

# Voltage waveform tailoring for high aspect ratio plasma etching of SiO<sub>2</sub> using Ar/CF<sub>4</sub>/O<sub>2</sub> mixtures: Consequences of low fundamental frequency biases

Cite as: Phys. Plasmas **31**, 033508 (2024); doi: 10.1063/5.0189397

Submitted: 28 November 2023 · Accepted: 5 March 2024 ·

Published Online: 29 March 2024



View Online



Export Citation



CrossMark

Florian Krüger,<sup>1,a)</sup>  Hyunjae Lee,<sup>2,b)</sup>  Sang Ki Nam,<sup>2,c)</sup>  and Mark J. Kushner<sup>1,d)</sup> 

## AFFILIATIONS

<sup>1</sup>Electrical Engineering and Computer Science Department, University of Michigan, 1301 Beal Ave., Ann Arbor, Michigan 48109-2122, USA

<sup>2</sup>Mechatronics R&D Center, Samsung Electronics Co., Ltd., 1-1 Samsungjeonja-ro, Hwaseong-si, Gyeonggi-do 18448, South Korea

**Note:** This paper is part of the Special Topic: Plasma Sources for Advanced Semiconductor Applications.

<sup>a)</sup>Electronic mail: [fkrueger@umich.edu](mailto:fkrueger@umich.edu)

<sup>b)</sup>Electronic mail: [hj0928.lee@samsung.com](mailto:hj0928.lee@samsung.com)

<sup>c)</sup>Electronic mail: [sangki.j.nam@samsung.com](mailto:sangki.j.nam@samsung.com)

<sup>d)</sup>Author to whom correspondence should be addressed: [mjkush@umich.edu](mailto:mjkush@umich.edu)

## ABSTRACT

The use of non-sinusoidal waveforms in low pressure capacitively coupled plasmas intended for microelectronics fabrication has the goal of customizing ion and electron energy and angular distributions to the wafer. One such non-sinusoidal waveform uses the sum of consecutive harmonics of a fundamental sinusoidal frequency,  $f_0$ , having a variable phase offset between the fundamental and even harmonics. In this paper, we discuss results from a computational investigation of the relation between ion energy and DC self-bias when varying the fundamental frequency  $f_0$  for capacitively coupled plasmas sustained in Ar/CF<sub>4</sub>/O<sub>2</sub> and how those trends translate to a high aspect ratio etching of trenches in SiO<sub>2</sub>. The fundamental frequency,  $f_0$ , was varied from 1 to 10 MHz and the relative phase from 0° to 180°. Two distinct regimes were identified. Average ion energy onto the wafer is strongly correlated with the DC self-bias at high  $f_0$ , with there being a maximum at  $\varphi = 0^\circ$  and minimum at  $\varphi = 180^\circ$ . In the low frequency regime, this correlation is weak. Average ion energy onto the wafer is instead dominated by dynamic transients in the applied voltage waveforms, with a maximum at  $\varphi = 180^\circ$  and minimum at  $\varphi = 0^\circ$ . The trends in ion energy translate to etch properties. In both, the high and low frequency regimes, higher ion energies translate to higher etch rates and generally preferable final features, though behaving differently with phase angle.

© 2024 Author(s). All article content, except where otherwise noted, is licensed under a Creative Commons Attribution (CC BY) license (<https://creativecommons.org/licenses/by/4.0/>). <https://doi.org/10.1063/5.0189397>

## I. INTRODUCTION

Plasma etching of dielectrics such as SiO<sub>2</sub> is an integral process in micro- and nanometer scale electronics fabrication.<sup>1</sup> The etching of high aspect ratio (HAR) features is becoming an increasingly critical process due to the development of three-dimensional structures such as 3D-NAND memory that requires vias (circular holes) through as many as 256 alternating layers of SiO<sub>2</sub> and Si<sub>3</sub>N<sub>4</sub> with a total aspect ratio of up to 100.<sup>2,3</sup> (Aspect ratio, AR, is the height of the feature divided by its width. AR > 10–20 would be considered HAR.) Plasma etching of HAR features requires highly energetic ions onto the wafer,

which arrive with a nearly normal angle. This anisotropy is achieved by acceleration of the ions through the electric field in the sheath bounding the wafer and normal to the surface. The majority of HAR plasma etching of dielectrics is performed in capacitively coupled plasmas (CCPs) sustained in fluorocarbon gas mixtures, typically using multiple radio frequency (RF) power supplies.<sup>4,5</sup>

Recent industry trends have favored the use of very low frequency (VLF) biases. VLFs, typically frequencies below 1–2 MHz, correspond to the thin sheath limit in which the ion entering the sheath will cross the sheath in a small fraction of the RF cycle. In this regime, maximum

ion energies incident onto the wafer extend to  $V_{RF}-V_{DC}$ , where  $V_{RF}$  is the amplitude of a sinusoidal bias and  $V_{DC}$  is the negative self-bias on the blocking capacitor. At the same time, the use of voltage waveform tailoring (VWT) is being investigated to customize those ion energy distributions. VWT consists of a bias which is the sum of multiple harmonic frequencies on a single electrode. Due to the added technical complexity and lack of fundamental understanding of its role in modifying ion and electron dynamics in and near the plasma sheath, VWT is only now being broadly adopted by industry.<sup>6–12</sup>

The DC self-bias,  $V_{DC}$ , is a voltage appearing on a blocking capacitor in series with the RF power supply.  $V_{DC}$  for conventional waveforms results from the requirement to balance positive and negative currents to both electrodes on a cycle averaged basis. These currents may not naturally balance due to differences in ion and electron mobility. This asymmetry may also be the result of geometry (differences in the areas of powered and unpowered surfaces), material (for example different electron emission coefficients), magnetic field configuration (different electron mobilities adjacent to powered and unpowered surfaces) and the use of asymmetric, non-sinusoidal, voltage waveforms for power coupling producing the electrical asymmetry effect (EAE). Through control of  $V_{DC}$ , control of the sheath potential and subsequently ion energies can be achieved.<sup>10,13,14</sup>

The direct measurement of ion energies during industrial plasma etching processes is usually not performed due to the added technical complexity or to avoid disturbing the plasma. As a result,  $V_{DC}$  is frequently used as a proxy for ion energy onto the wafer. This is a good approximation if the sheath is collisionless and the system is operating in the thick sheath limit, where the ion requires many RF cycles to cross the sheath. For these conditions, the ion energy distribution (IED) striking the wafer has a narrow width in energy centered on  $-V_{DC}$ . This is typically the condition intended for control of the IED through VWT.

In this paper, we discuss results from a computational investigation into the relationship between  $V_{DC}$  and the IED for capacitively coupled plasmas employing VWT over a large range of fundamental bias frequencies. The computed reactive fluxes to the substrate and their energy distributions were used as input to a profile simulator to assess the influences of these reactive fluxes on HAR features etched into  $\text{SiO}_2$ . We found that at very low frequencies, the ions are able to dynamically react to the applied potential, and as a consequence, incident ion energy onto the wafer can decouple from the trends suggested by  $V_{DC}$ .

Brief descriptions of reactor and feature scale models employed in this investigation are presented in Sec. II. The results of the reactor scale gas phase simulations are presented and discussed for constant bias voltage amplitude in Sec. III and for constant bias power in Sec. IV. The results for simulated profiles of HAR trenches etched in  $\text{SiO}_2$  using the reactive fluxes produced by these waveforms are discussed in Sec. V. Concluding remarks are presented in Sec. VI.

## II. DESCRIPTION OF THE MODELS

### A. Reactor scale model

The investigation of the reactor scale plasma dynamics was performed using the Hybrid Plasma Equipment Model (HPEM),<sup>15–17</sup> which is described in detail in Ref. 18. A brief overview of the HPEM is given here. The HPEM is a two-dimensional plasma hydrodynamics model, which resolves transport phenomena using a time-slicing

approach. Different physics regimes are addressed in modules that are coupled by exchanging physical quantities—electric and magnetic fields, densities, and rate coefficients. The major modules used in this work are the Fluid Kinetics-Poisson Module (FKPM), the Electron Energy Transport Module (EETM), and the Plasma Chemistry Monte Carlo Module (PCMCM). In the FKPM, the continuity, momentum, and energy equations of heavy particles are solved coincidentally with Poisson's equation to provide heavy particle densities, fluxes, temperatures, and electrostatic potential. Continuity and momenta are solved for electron transport. Although the fluid treatment for ions that is used to obtain convergence is not kinetic, including continuity, momentum, and energy equations for each species does represent a non-local treatment. This non-local behavior is particularly important in determining ion transport flowing into the sheath.

The temperatures of individual neutral species and ions are computed by considering local contributions due to Joule heating (for ions), charge exchange heating for neutrals and cooling for ions, elastic collisions of electrons, exothermic and endothermic neutral reactions, and Franck-Condon heating in dissociative electron impact processes including dissociative recombination and elastic collisions between heavy particles. Non-local contributions to gas heating include convective transport and thermal conduction. The gas and ion temperatures impact the calculations through temperature dependent rate coefficients, rarefaction of gas densities, and the random thermal velocities of ions that enter the sheath, which partially determine the angular distribution of ions striking the wafer.

In the EETM, the spatially dependent electron energy distributions (EEDs) are obtained using a kinetic, Monte Carlo based approach utilizing the space and phase resolved electric fields produced in the FKPM. The HPEM accounts for two classes of electrons. Bulk electrons, whose origins are electron impact ionization, have densities that are modeled as a fluid in the FKPM with energy distributions determined by the kinetic Monte Carlo simulation in the EETM. The second class includes electrons that originate from secondary electron emission from the surfaces and subsequent acceleration in the sheath. These are typically energetic beam-like electrons whose densities and velocities are tracked kinetically. The beam electrons deposit their energy back into the system through collisions and are a source of bulk electrons once their energy falls below the minimum inelastic threshold energy for electron impact excitation.

In the EETM, the energy and angular distribution (EAD) of electrons striking the substrate are recorded. Using the EEDs in the bulk plasma, electron transport and rate coefficients are obtained, which are transferred to the other modules. After the plasma reaches a quasi-steady state in the PCMCM, the trajectories of ions and reactive neutral species are tracked using Monte Carlo techniques. Energy and angular distributions (EADs) of these species are recorded impinging onto the wafer. The reaction mechanism used for  $\text{Ar/O}_2/\text{CF}_4$  plasmas is described in Huang *et al.*<sup>19</sup> The mechanism contains the following heavy particle species:

Rare gas: Ar,  $\text{Ar}(4s[3/2]_2)$ ,  $\text{Ar}(4s[3/2]_1)$ ,  $\text{Ar}(4s'[1/2]_0)$ ,  $\text{Ar}(4s'[1/2]_1)$ ,  $\text{Ar}(4P)$ ,  $\text{Ar}(4D)$ , and  $\text{Ar}^+$   
 Fluorocarbon:  $\text{CF}_4$ ,  $\text{CF}_3$ ,  $\text{CF}_2$ , C,  $\text{CF}_3^+$ ,  $\text{CF}_2^+$ ,  $\text{CF}^+$ ,  $\text{C}^+$ , and  $\text{CF}_3^-$   
 Oxygen:  $\text{O}_2$ ,  $\text{O}_2^*$ , O,  $\text{O}^*$ ,  $\text{O}_2^+$ ,  $\text{O}^+$ , and  $\text{O}^-$ ,  
 Fluorine:  $\text{F}_2$ , F,  $\text{F}^*$ ,  $\text{F}_2^+$ ,  $\text{F}^+$ , and  $\text{F}^-$   
 Reaction and etch products:  $\text{SiF}_4$ ,  $\text{SiF}_3$ ,  $\text{SiF}_2$ , CO, COF,  $\text{COF}_2$ ,  $\text{CO}_2$ , FO, and  $\text{CO}^+$

Ion species impinging on surfaces generate secondary electrons based on fixed energy independent coefficients. The secondary electron emission coefficient was 0.15 for the wafer and metal and 0.05 for the dielectric covered walls.<sup>19</sup> Excited states of argon and fluorine had a secondary emission coefficient of 0.01 on all surfaces.<sup>20</sup> All ions recombine on surfaces to form their neutral counterparts.

A schematic of the cylindrically symmetric CCP reactor used in this investigation is shown in Fig. 1. The reactor, modeled after multi-frequency CCPs used in industrial plasma etching applications, consists of two parallel plate electrodes with a diameter of 30 cm separated by a 2.8 cm gap. A silicon wafer is mounted on the bottom electrode and a showerhead gas inlet is distributed across the top electrode. A focus ring made of quartz to improve uniformity of fluxes to the wafer surrounds the substrate. The dielectric constant of the quartz ring is  $\epsilon/\epsilon_0 = 4$ . The conductivity of the quartz ring is negligible while that of the Si wafer is  $0.05/\Omega\text{ cm}$ . The feedstock gas is an  $\text{Ar}/\text{CF}_4/\text{O}_2 = 75/15/10$  mixture flowing at 500 sccm through the showerhead. The reactor pressure is held constant at 40 mTorr at the location of a pressure sensor near the pump port. This is accomplished by throttling the rate of pumping.

Voltage waveform tailoring (VWT) is provided by a power supply connected to the bottom electrode through a blocking capacitor of 100 nF. As such, we are not addressing distortion of the waveform originating from the power supply that may occur by the impedance of the transmission line and substrate. In quasi-steady state operation, the value of  $V_{\text{DC}}$  should be independent of the value of the blocking capacitor provided that the RC time constant of the plasma-capacitor series impedance is large compared to transients in current. The capacitance used here is a balance of there being an acceptably short charging time and long enough RC time constant so that there is little variation in the  $V_{\text{DC}}$  during the RF cycle.

The plasma is largely sustained by a sinusoidal voltage with amplitude  $V_T$  applied to the top electrode with a fundamental frequency of 80 MHz. To control the dynamics of charged particles impinging on the wafer surface, a customized voltage waveform,  $V(t)$ , is applied to the bottom electrode. The waveform consists of a fundamental sine wave with a frequency  $f_0 = 1\text{--}10$  MHz and four consecutive higher harmonics

$$V(t) = V_0 \sum_{k=1}^N \frac{N-k-1}{N(N+k)} \cos(2k\pi f_0 t + k\pi\phi_k). \quad (1)$$

Here,  $V_0$  is the total applied voltage amplitude,  $k$  is the harmonic order,  $N$  is the total number of frequencies, and the relative phase shift of each harmonic frequency  $k$  is  $\phi_k$ . In this work, the number of harmonics is  $N = 5$ . The consequences of VWT were investigated by varying the phase shift of the even harmonics  $\phi$  for  $k = 2$  and 4. The resulting waveforms are shown in Fig. 2 for phase shifts of  $\phi = 0^\circ, 45^\circ, 90^\circ, 135^\circ,$  and  $180^\circ$ . With the shape and frequency of the applied voltage being closely linked to the plasma properties, two scenarios were investigated:

- (a) Voltages are held constant at  $V_T = 300$  and  $V_0 = 1500$  V, as phase shift  $\phi$  and fundamental frequency  $f_0$  are varied.
- (b) Applied voltages are dynamically adjusted to maintain a constant power deposition of  $P_T = P_B = 2000$  W.

### B. Feature scale model

The fluxes and particle energy and angular distributions to the wafer obtained from HPEM are used as input to the Monte Carlo Feature Profile Model (MCFPM) to simulate the evolution of etch features in semiconductor device materials.<sup>21,22</sup> The MCFPM is a voxel-based, kinetic model in which pseudo-particles representing gas phase species are launched with energies and angles sampled from the distributions obtained from the HPEM. The trajectories of the incoming particles are advanced according to their initial velocity and their acceleration by electric fields produced by feature charging until a collision with a surface occurs. Due to the low density of reactive particles in a feature (typically only one particle at any given time) and long mean free path for collisions with background gases, collisions of the pseudo-particles with other gas phase species are not considered. Upon striking a surface, and based on the particle's incident energy and angle, a Monte Carlo technique is employed to determine the specific reaction that occurs. The state of the surface voxel is changed according to the reaction that is selected. The voxel can be removed (physical or chemical sputtering), replaced (chemical modification), or a voxel is added on top of the site (deposition). If the reaction yields a non-saturated or reactive gas phase species, a new gas phase pseudo-particle is launched from that site.

The mechanism for etching of  $\text{SiO}_2$  in an  $\text{Ar}/\text{O}_2/\text{CF}_4$  gas mixture used in this work is described in Ref. 21. All incoming ions neutralize and deposit their charge during the first wall collision while retaining a fraction of their energy upon reflection. These particles are then called "hot neutrals." All ions and hot neutrals striking surfaces can physically sputter all materials according to the incident particle's mass, angle, and energy as well as the surface binding energy of the material. The formation of a complex between fluorocarbon radicals and  $\text{SiO}_2$  lowers the binding surface energy, thereby reducing the chemical sputtering threshold.  $\text{C}_x\text{F}_y$  radicals deposit a thin polymer layer (at most a few nm), which is the primary source of sidewall passivation within the feature, whose thickness is controlled by etching with oxygen radicals.

To demonstrate the consequences of changes of ion energy and angular distributions (IEADs) resulting from varying  $f_0$  and phase angle, simulations were performed of etching a trench through

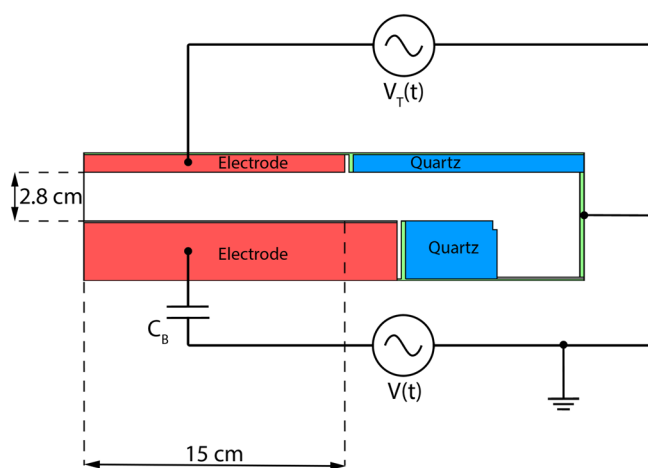


FIG. 1. Reactor geometry and circuit diagram.

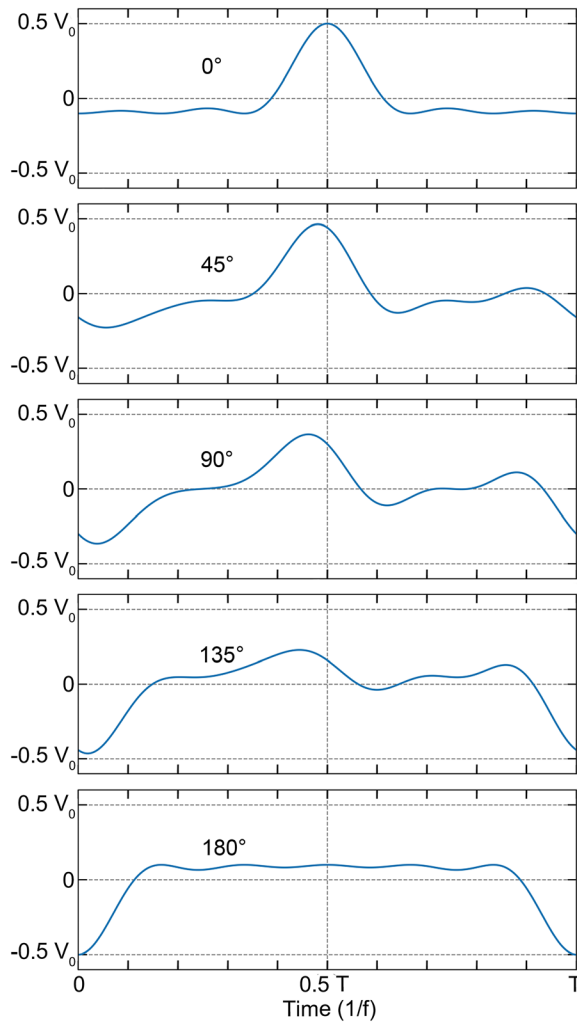


FIG. 2. Voltage waveforms corresponding to phase shifts of  $\varphi = 0^\circ$  to  $180^\circ$ .

3000 nm of SiO<sub>2</sub> covered by a 700 nm thick mask with a 100 nm opening; and terminated by a 100 nm thick Si stop layer. The total aspect ratio is approximately 30. The geometry used for the feature evolution is shown in Fig. 3. The simulation was performed in three dimensions with a mesh consisting of 60 cells wide by 750 cells tall by 20 cells deep using periodic boundary conditions, producing cubic voxels with a 5 nm side length. The etching was performed for a fixed time of 10 min.

The intent of the simulation is a uniform trench perpendicular to the plane shown in Fig. 3 which could, in principle be performed in two dimensions. However, we have found that more robust results are produced when performing a finite depth three-dimensional simulation. In two dimensions, roughness or statistical variation in surface properties are extended infinitely into the third dimension, which can systematically prejudice the outcome, for example, overemphasizing twisting. The finite depth 3D simulations, even with periodic boundary conditions, largely removes these systemic biases.

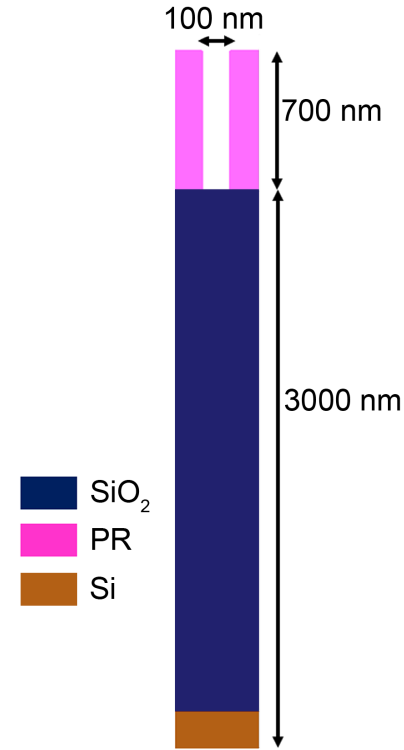
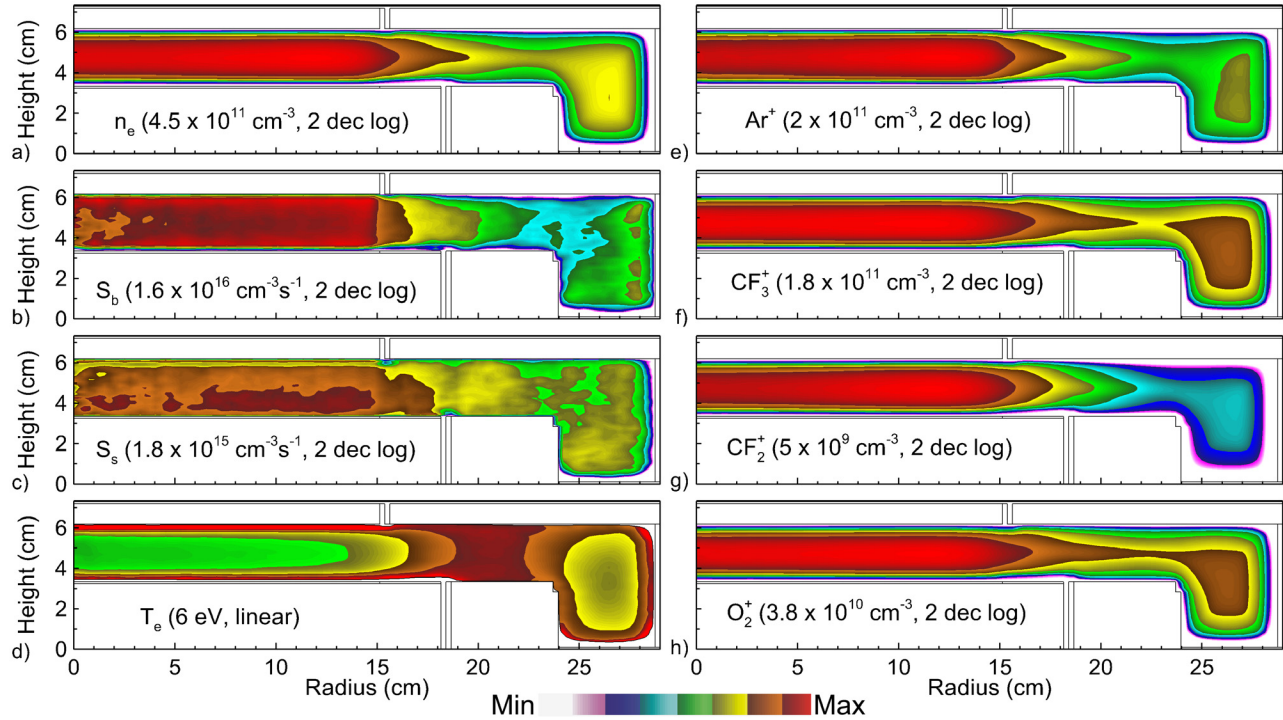


FIG. 3. Feature scale model initial conditions for simulating plasma etching of SiO<sub>2</sub>. PR represents photoresist.

### III. REACTOR SCALE PLASMA PROPERTIES WITH CONSTANT APPLIED VOLTAGE

With constant applied voltage amplitudes of  $V_T = 300$  and  $V_0 = 1500$  V, the fundamental frequency  $f_0$  was varied from 1 to 10 MHz. For each frequency, a sweep across the phase angle  $\varphi$  was performed with  $\varphi = 0^\circ, 45^\circ, 90^\circ, 135^\circ,$  and  $180^\circ$ . The electron density for the base case with  $f_0 = 1$  MHz and  $\varphi = 0^\circ$  is shown in Fig. 4(a). The cycle averaged electron density at mid-gap is  $4.5 \times 10^{11} \text{ cm}^{-3}$ , sustained by an electron temperature of 3.1 eV. Ionization at mid-gap is approximately 90% by bulk electrons and 10% by secondary, sheath accelerated electrons. Electron density  $n_e$  and temperature  $T_e$  are fairly homogeneous as a function of radius as shown in Figs. 4(a) and 4(d). The spatial electron source distribution, generated by bulk electrons  $S_b$ , closely resembles those of  $n_e$  and  $T_e$ , as shown in Fig. 4(b). The smaller, but still significant amount of ionization by secondary electrons  $S_s$  is shown in Fig. 4(c). Since the bulk ionization source is mostly a consequence of electrons accelerated by sheath motion, its maximum is located at the sheath edges.  $S_s$  results from electrons accelerated by the total sheath potential and is maximum close to the bottom electrode. The dominant positive ions ( $\text{Ar}^+, \text{CF}_3^+, \text{CF}_2^+,$  and  $\text{O}_2^+$ ) are also shown in Fig. 4. The spatial distribution of these ions are similar, with the lower ionization potential species ( $\text{CF}_3^+, \text{CF}_2^+,$  and  $\text{O}_2^+$ ) having a broader spatial distribution to larger radii. These distributions result from charge exchange depleting  $\text{Ar}^+$  as the ions diffuses radially outward from where electron impact ionization dominantly occurs over



**FIG. 4.** Plasma properties of the Ar/CF<sub>4</sub>/O<sub>2</sub> CCP base case with  $V_T = 300$  V,  $V_0 = 1500$  V,  $f_0 = 1$  MHz, and  $\varphi = 0^\circ$ . Time averaged (a) electron density  $n_e$ , (b) ionization source by bulk electrons  $S_b$ , (c) ionization source by secondary electrons  $S_s$ , (d) electron temperature,  $T_e$ , and ion densities, (e) Ar<sup>+</sup>, (f) CF<sub>3</sub><sup>+</sup>, (g) CF<sub>2</sub><sup>+</sup>, and (h) O<sub>2</sub><sup>+</sup>.

the wafer. The neutral gas temperature (averaged over species) has a maximum value of 580 K and reactor average value of 450 K.

The different voltage waveforms that result from changing the phase angle  $\varphi$  can alter the discharge dynamics through differences in sheath expansion heating, electron confinement and modifying surface processes such as ion and electron induced secondary electron emission. While the constant sinusoidal voltage applied to the top electrode is meant to provide a constant background ionization and electron heating, some variation in electron density  $n_e$  as a function of  $\varphi$  nevertheless occurs and is shown in Fig. 5 for fundamental frequencies  $f_0 = 1$ –10 MHz. Generally,  $n_e$  is a function of the total input power at frequencies that produce electron heating. With the top electrode powered at 80 MHz, the majority of this power is expended in electron heating. With varying harmonic content with changing  $\varphi$  on the bottom electrode, power deposition into electrons also varies, directly translating to changes in electron heating and ionization.

The decrease in electron density with increasing phase angle is at least partially the consequence of less efficient electron confinement. Electrons are largely confined to the bulk plasma by electric fields in the sheaths which point toward surfaces during the majority of the RF cycle. Electrons typically reach the surface (to balance positive ion current) by diffusion across the sheath during a short period during the anodic portion of the cycle. If transport by diffusion is insufficient to balance currents, an electric field reversal may occur to accelerate electrons toward the surface.<sup>23</sup> For  $\varphi = 0^\circ$  (peak waveform), the plasma sheath is nearly at its maximum width with the most negative sheath potential for the majority of the RF cycle, allowing electron transport to the surface only during the brief collapse in the sheath at the peak of

the anodic portion of the cycle. The opposite is true for  $\varphi = 180^\circ$  where the plasma sheath is collapsed (anode-like) for most of the RF period, allowing electrons to transport to the bottom surface for a significantly longer fraction of the cycle.

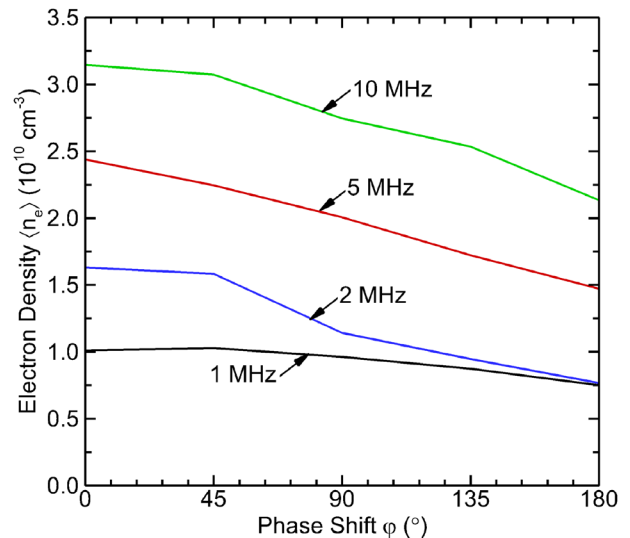


**FIG. 5.** Average electron density as a function of phase shift  $\varphi$  for fundamental frequencies  $f_0 = 1$ –10 MHz at constant applied voltage.

With constant voltage ( $V_T = 300$  and  $V_0 = 1500$  V), power deposition from the top electrode is a function of the bulk plasma properties and not independent of the bottom electrode power coupling. Power deposition as a function of phase angle  $\varphi$  and fundamental frequency  $f_0$  are shown in Fig. 6(a) for the top electrode ( $P_T$ ) and Fig. 6(b) for the bottom electrode ( $P_0$ ). Higher fundamental frequencies  $f_0$  on the bottom electrode produce more efficient electron heating and higher power deposition for a fixed voltage. For our conditions, electron power deposition is dominated by stochastic heating resulting from sheath expansion (or sheath speed) which is more rapid and occurs more often at higher frequencies. Increasing the fundamental frequency  $f_0$  of the voltage on the bottom electrode, therefore, leads to a significant increase in power deposition,  $P_B$ . However, this relation is non-linear. A tenfold increase in frequency  $f_0$  (1–10 MHz) only results in a 1.5 ( $\varphi = 180^\circ$ ) to 2 ( $\varphi = 0^\circ$ ) increase in  $P_B$ . These trends in power deposition with frequency directly translate to the corresponding

trends in  $n_e$  as shown in Fig. 5. Smaller phase angles have more rapidly expanding sheaths producing more electron heating, leading to an increase in  $P_B$ . With constant top voltage  $V_T$ , additional electron heating produced by  $P_B$  which increases electron density translates to an increase in power deposition by the top electrode,  $P_T$ .

Earlier works have described the dependence of  $V_{DC}$  on the shape of the applied waveform through the generation of the electrical asymmetry effect (EAE).<sup>24,25</sup> Given these dependencies,  $V_{DC}$  can be expressed as

$$V_{DC} = -\frac{V_{max} + \beta V_{min}}{1 + \beta}, \quad (2)$$

where  $V_{max}$  and  $V_{min}$  are the maximum and minimum of the applied voltage.  $\beta$  is the discharge symmetry parameter given by

$$\beta = \left(\frac{A_p}{A_g}\right)^2 \frac{\bar{n}_{sp} I_{sg}}{\bar{n}_{sg} I_{sp}}, \quad (3)$$

where the areas of the powered and ground electrodes are  $A_p$  and  $A_g$  and the ion densities near the powered and grounded surfaces are  $\bar{n}_{sp}$  and  $\bar{n}_{sg}$ .  $I_{sp}$  and  $I_{sg}$  are the sheath integrals, described in prior works discussing the theory of the EAE.<sup>13,24,26</sup> This relation implies that the magnitude of  $V_{DC}$  is largest (most negative) for  $\varphi = 0^\circ$  and decreases with increasing  $\varphi$  (becoming more positive). The precise phases for which the extrema occur in  $V_{DC}$  are likely sensitive to the geometry of the reactor, which determines the relative contributions of displacement and conduction current that ultimately flows to the powered electrode. The values of  $V_{DC}$  produced by the model, shown in Fig. 7(a) as a function of phase shift  $\varphi$  for fundamental frequencies  $f_0 = 1, 2, 5,$  and  $10$  MHz, generally verify this scaling.  $|V_{DC}|$  tends to decrease with increasing  $\varphi$  for all frequencies (the negative  $V_{DC}$  becoming more positive).

An exception to this trend for  $V_{DC}$  occurs for  $f_0 = 1, 2$  MHz,  $\varphi = 180^\circ$  for which magnitude of  $V_{DC}$  decreases slightly. These exceptions are likely due to effects such as contributions of  $V_{DC}$  to secondary electron emission produced ionization, relative contributions of conduction current and displacement current in a geometrically complex reactor and electronegativity of the plasma which are not explicitly included in the theory leading to Eq. (2). The current that flows into the blocking capacitor through the metal substrate contains contributions of conduction current flowing through, for example, a conductive wafer and displacement current that enters through the side of the substrate that is covered by the dielectric focus ring. This displacement current originates from conduction current that charges the surface of the focus ring. However, the current that flows through the dielectric to the underlying electrode is displacement current.

The mean ion energies striking the wafer are shown in Fig. 7(b) as a function of phase shift  $\varphi$  for fundamental frequencies  $f_0 = 1, 2, 5,$  and  $10$  MHz. Mean ion energy is the unweighted arithmetic average of all ions striking the wafer. The expectation is that mean ion energy should closely track the magnitude of  $V_{DC}$  with a change in phase shift  $\varphi$ . This expectation is met for the highest frequency 10 MHz. At lower frequencies, beginning with 5 MHz, the correlation of mean ion energy with magnitude of  $V_{DC}$  as a function of phase shift  $\varphi$  begins to break down. At 1 MHz, the mean ion energy increases with phase shift while magnitude of  $V_{DC}$  is constant or is decreasing.

Recall that  $V_{DC}$  results from the requirement that the current flowing to each electrode (powered and grounded) be equal over the

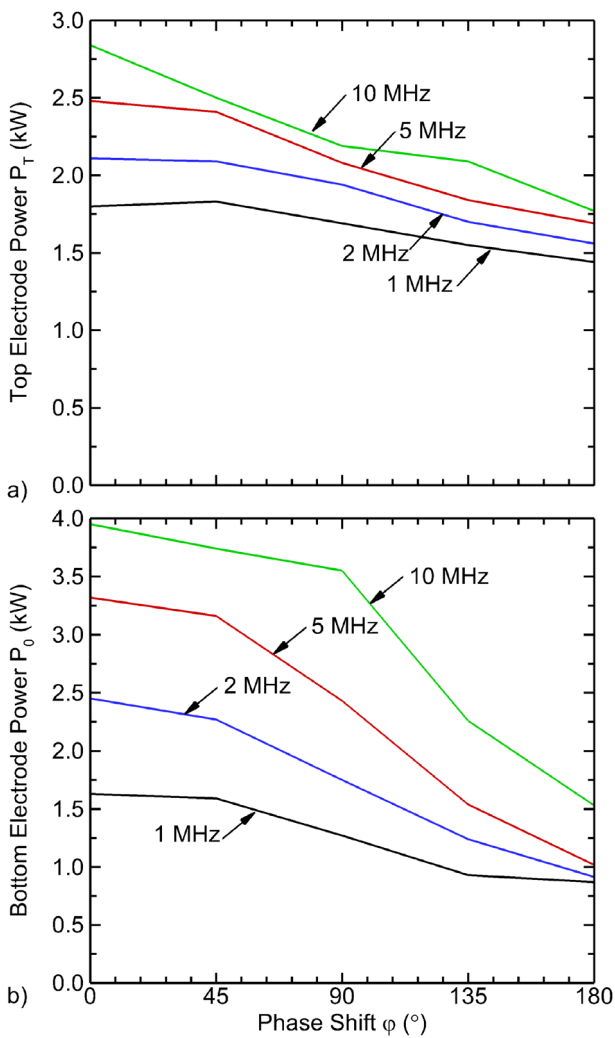
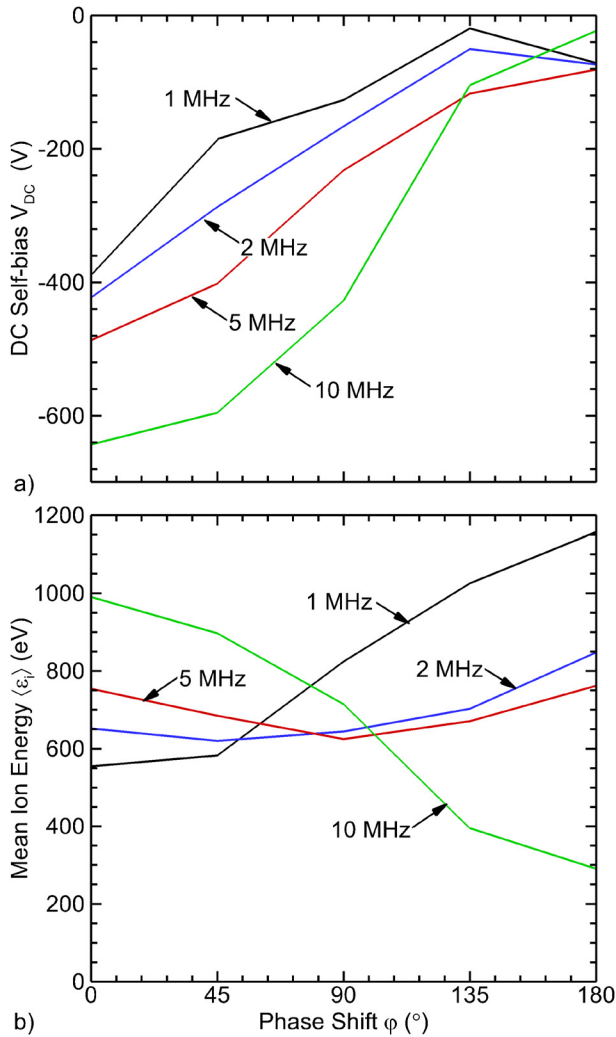


FIG. 6. Power deposition for (a) top electrode and (b) bottom electrode as a function of phase shift  $\varphi$  for fundamental frequencies  $f_0 = 1$ –10 MHz.



**FIG. 7.** Plasma properties as a function of phase shift  $\phi$  for different fundamental frequencies  $f_0 = 1$ –10 MHz for constant voltage. (a)  $V_{DC}$ . (b) Mean ion energy incident onto the wafer.

RF cycle. In our model, currents are computed at the electrode surface. If that surface is in direct contact with the plasma, the current consists of both conduction current (charged particles flowing to the surface) and displacement current ( $\vec{j}_D = \partial(\epsilon\vec{E})/\partial t$ ). If the electrode is in contact with a conductive material that is in contact with the plasma, such as the wafer, the current collected by the electrode consists of conduction current (through the wafer) and displacement current. If the electrode is buried beneath or within non-conducting dielectrics, the current the electrode collects is only displacement current. Contributions of displacement current to the bottom electrode may originate from charging of the top and sides of the focus ring. With the ratio of conduction to displacement current being functions of frequency which differs for top and bottom electrodes, there is no expectation that  $V_{DC}$  should be independent of frequency.

Another factor that may affect  $V_{DC}$  with frequency is electron heating. With electron heating being dominated by sheath expansion,

higher bias frequencies  $f_0$  produce more electron heating adjacent to the sheath at the bottom electrode for any given voltage amplitude. With increasing  $f_0$  this increase in local as well as bulk electron density  $n_e$  leads to a decrease in shielding lengths  $\lambda_D$  and a decrease in the sheath width  $d_s$  at the bottom electrode. The end result is a change the ratio of surface adjacent ion densities ( $n_{sp}/n_{sg}$ ). As described by Eqs. (2) and (3), this change directly translates to a change in the  $V_{DC}$ .

An ion's ability to react to temporally changing electric fields in the sheath is related to the time required for the ion to cross the sheath,  $\Delta T$ , compared to the RF period,  $1/\nu_{RF}$ , described by the sheath ion inertia coefficient,

$$S = \Delta T \nu_{RF} = \nu_{RF} \left( \frac{2d_s^2 m_i}{qV_S} \right)^{1/2}, \quad (4)$$

where  $d_s$  is the average sheath thickness,  $V_S$  is the average sheath potential,  $m_i$  is the ion mass, and  $q$  is the elementary charge. For  $S > 1$ , ions typically do not dynamically respond to changes in the electric field that occur in the sheath (high frequency, large mass, and thick sheath). Ions transiting through sheaths whose oscillation frequency produces  $S \gg 1$  arrive at the surface with an energy close to the average sheath potential. Although this scaling assumes a sinusoidal voltage with a single ion species, it can nevertheless serve as a general guide to understanding the frequency dependent trends in average ion energy onto the wafer shown in Fig. 7(b).

$S$  depends on the value of the sheath width. Defining a precise criterion for location of the sheath-bulk plasma transition is an active area of research<sup>27–36</sup> and beyond the scope of this work. In this work, the sheath edge is defined as the location at which the sheath electric field has decayed to  $10^{-3}$  of its maximum value. The resulting sheath thickness is shown in Fig. 8(a) as a function of the fundamental frequency  $f_0$  with  $\phi = 0^\circ$ . Since the sheath thickness is generally inversely proportional to plasma density at the sheath edge, which increases with  $f_0$ , the sheath thickness decreases with increasing frequency.  $S$  as a function of  $f_0$  for  $\phi = 0^\circ$  is shown in Fig. 8(b). Consistent with the premise above, non-dynamic ion transport through the sheath with  $S > 1$  occurs for  $f_0 = 10$  MHz. Dynamic transport behavior where ions react to time variations of electric field in the sheath with  $S < 1$  occurs for  $f_0 = 1$  MHz. As such, at the high end of frequencies, the ion dynamics are dominated by time averaged sheath properties, such as the DC self-bias,  $V_{DC}$ . It is for that reason that mean ion energy as a function of phase angle for  $f_0 = 10$  MHz scales proportionally to the magnitude of  $V_{DC}$ , as shown in Fig. 7(b).

Moving to lower fundamental frequencies  $f_0$ , the trend for average ion energy as a function of phase angle  $\phi$  reverses. At low  $f_0$ , the average ion energy increases with increasing  $\phi$ . Lowering the fundamental frequency results in the sheath modulation time scales approaching a regime in which ions can dynamically react to transients in the electric fields. For example, compare the voltage waveforms shown in Fig. 2 for  $\phi = 0^\circ$  (peak) and  $\phi = 180^\circ$  (valley). Assuming dynamically reacting (positive) ions ( $S < 1$ ), the maximum ion flux to the electrode occurs when the applied voltage is most negative. At  $\phi = 0^\circ$ , the applied potential is negative with respect to the plasma for most of the RF period. However, the minimum sheath potential,  $V_{min}$ , has a smaller magnitude than for  $\phi = 180^\circ$ . It is this ability of the ions to (at least partially) react to applied voltage transients that results in their incident energy onto the surface to scale with the DC self-bias at

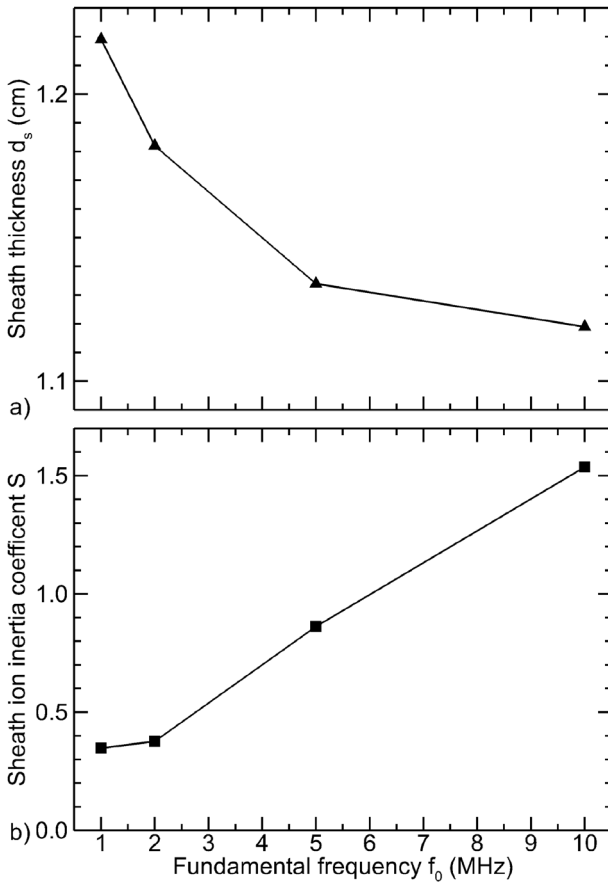


FIG. 8. Sheath properties as a function of fundamental frequency  $f_0$  for  $\varphi = 0^\circ$  at constant voltage. (a) Sheath thickness  $d_s$  and (b) sheath ion inertia coefficient S.

high frequencies and the applied minimum potential at low frequencies.

The incident average energies of select ion species as a function of atomic mass for  $f_0 = 10$  MHz and  $\varphi = 180^\circ$  are shown in Fig. 9(a). The ion energy and angular distributions corresponding to these mean energies are shown in Fig. 9(b). Due to their lower inertia, the lighter  $O^+$  ions can more rapidly react to changes in the electric field than heavier species such as  $CF_3^+$ . Consequently, the lighter ions can reach an energy closer to the maximum sheath potential drop during the small fraction of the RF period when the potential is most negative and have broader energy distributions. While the average ion energies differ by approximately 60 eV which is only about 5% of the total, these trends illustrate the relation between the average ion energy and the ion's ability to dynamically react to transient fields. That said, although the mean energies are similar, the IEADs are quantitatively different as a function of mass. These differences are highlighted by the two-decade log scale used in Fig. 9(b). As there are energy dependencies to surface reactions, there would be somewhat more sensitivity in total rates of reaction than indicated solely by mean energy.

This scaling is also shown by the trends in the IEADs collected at the wafer surface shown in Fig. 10 for  $f_0 = 1$  and 10 MHz for phase shifts  $\varphi = 0^\circ, 45^\circ, 90^\circ, 135^\circ,$  and  $180^\circ$ . The IEADs represent the sum

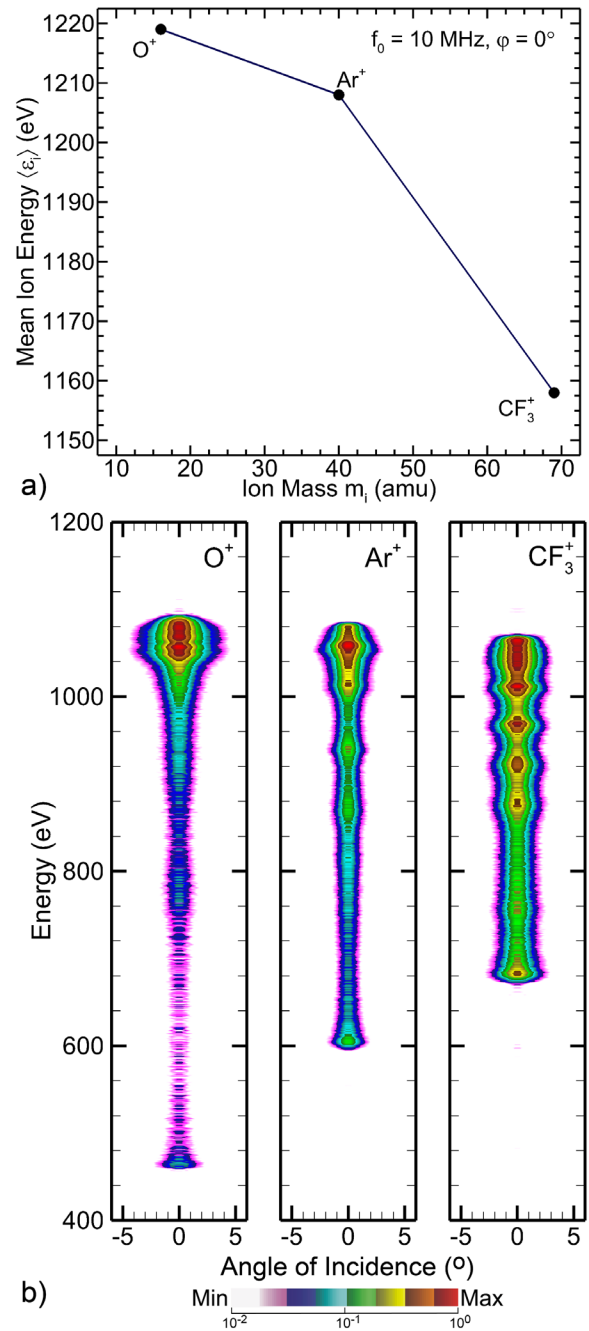
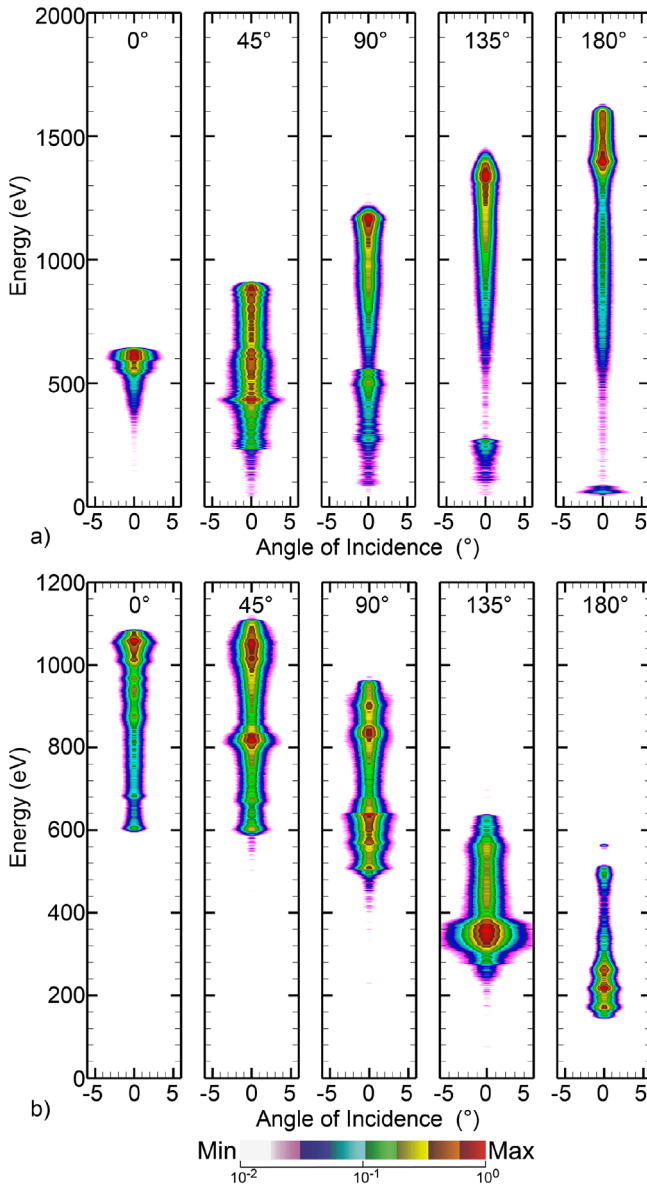


FIG. 9. Incident ion species as a function of mass for  $f_0 = 10$  MHz and  $\varphi = 0^\circ$ . (a) Mean ion energy and (b) ion energy and angular distribution (two-decade log scale).

of the fluxes of all positive ions. At the lowest frequency, the increase average energy with  $\varphi$  is mirrored in the IEAD where the mean energy is roughly equal to  $-V_{DC} - |V_{min}|$ .

As with the average energies onto the surface, there are significant differences in the trends for IEADs as a function of  $\varphi$  between the low



**FIG. 10.** IEADs as a function of phase shift  $\varphi$  for fundamental frequencies (a)  $f_0 = 1$  MHz and (b)  $f_0 = 10$  MHz at constant applied voltage. Values are plotted on a two-decade log scale.

and high fundamental frequencies. Overall, with  $f_0 = 10$  MHz, both maximum and average energies trend downwards with increasing  $\varphi$  while maintaining an approximately constant spread in energy.

Two distinct regimes for the behavior of average ion energy and IEAD with respect to the phase angle (and  $V_{DC}$ ) can be defined: The first is the *steady state ion regime* having  $S > 1$  (large  $f_0$ ) in which average ion energy onto the surface is well correlated with the magnitude of  $V_{DC}$ , with the average energy being maximum at  $\varphi = 0^\circ$  and minimum at  $\varphi = 180^\circ$ . The second is the *dynamic ion regime* having  $S < 1$  (small  $f_0$ ) where average ion energy and the IEAD are dominated by

the temporal response of the ions to the applied voltage waveforms—with the average ion energy being minimum at  $\varphi = 0^\circ$  and maximum at  $\varphi = 180^\circ$ .

**IV. REACTOR SCALE PLASMA PROPERTIES WITH CONSTANT APPLIED POWER**

To better align with industry practice where power (as opposed to voltage) is the control variable, simulations were performed in which the total power deposition was held constant for both electrodes while varying frequency and phase angle of the waveform on the bottom electrode. This was achieved by adjusting the voltage on the top electrode,  $V_T$ , and bottom electrode,  $V_0$ , to deliver power depositions of  $P_T = P_0 = 2000$  W.

The voltage amplitudes applied to the top electrode  $V_T$  are shown in Fig. 11(a) as a function of phase shift  $\varphi$  for fundamental frequencies  $f_0 = 1-10$  MHz. The mean electron density as a function of  $\varphi$  for

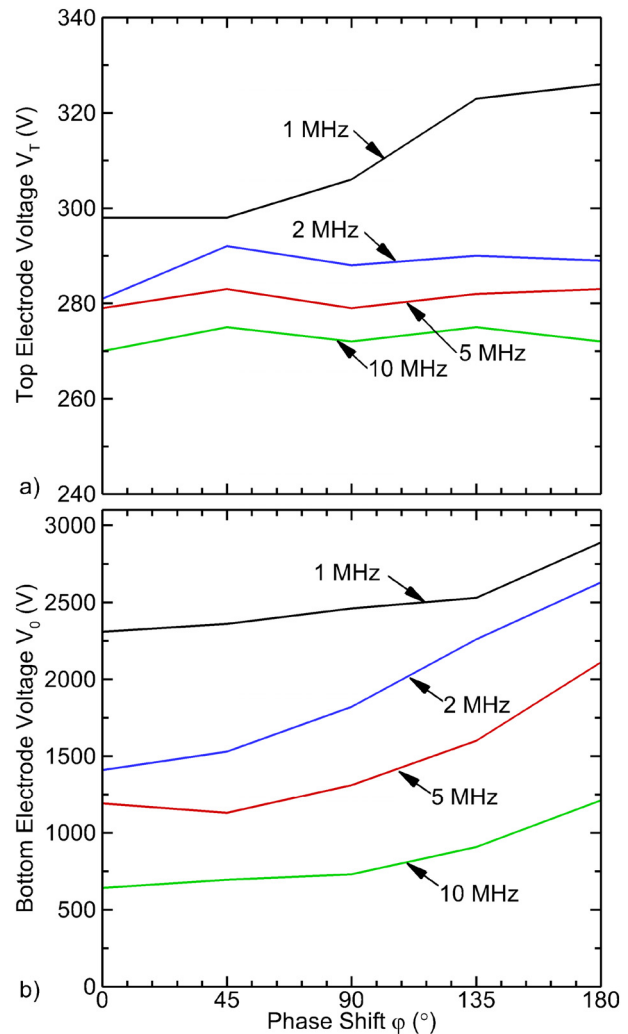


**FIG. 11.** Applied voltage for constant power (2000 W) as function of phase shift  $\varphi$  for fundamental frequencies  $f_0 = 1-10$  MHz applied to the bottom electrode. (a) Top electrode and (b) bottom electrode.

01 April 2024 12:15:40

$f_0 = 1\text{--}10\text{ MHz}$  is shown in Fig. 12. When delivering constant power,  $V_T$  is a weak function of  $\varphi$  for a given  $f_0$ . However, the  $V_T$  decreases with increasing  $f_0$ . For a given  $f_0$  with power delivered though the bottom electrode being held constant, the plasma density and so total impedance of the system does not significantly vary with  $\varphi$ . Consequently, the change in  $V_T$  with  $\varphi$  to deliver constant power is small. However, with increasing  $f_0$ , the fraction of power delivered by the bottom electrode devoted to ion acceleration decreases and that delivered to electron heating increases, which for constant power, produces an increase in electron density and decrease in impedance. A lower  $V_T$  is then required to deliver constant power.

The voltage applied to the bottom electrode,  $V_0$ , with respect to  $f_0$  and  $\varphi$  is shown in Fig. 11(b) for constant power deposition. Power deposition for constant voltage and  $f_0$  generally decreases with increasing  $\varphi$ , as shown in Fig. 5. To recoup this decrease in power to maintain constant power,  $V_0$  increases with increasing  $\varphi$ . The thickness of the sheath adjacent to the bottom electrode  $d_s$  and the sheath ion inertia coefficient  $S$  as a function of  $f_0$  are shown in Fig. 13 for  $\varphi = 0^\circ$  at constant voltage. With  $d_s$  being a function of the electron density which increases with  $f_0$ , the sheath thickness decreases. This reduction in  $d_s$  contributes to a decrease in  $S$ . However, this effect is dominated by the changes in  $f_0$  and  $V_s$ , ultimately resulting in an increase in  $S$  with  $f_0$ . This trend indicates that with constant power, a transition also occurs from the steady state ion regime to the dynamic ion regime occurs as a function of  $f_0$ .

The DC self-bias  $V_{DC}$  as a function of phase angle  $\varphi$  for  $f_0 = 1\text{--}10\text{ MHz}$  is shown in Fig. 14(a) while maintaining constant power. The trends with  $\varphi$  are similar those when keeping voltage constant, shown in Fig. 6(a), where the magnitude of  $V_{DC}$  decreases (becomes more positive) with  $\varphi$  due to the electrical asymmetry effect. However, when holding power constant, the amplitude of  $V_0$  decreases with increasing  $f_0$  due to there being a larger proportion of power being more efficiently dissipated by electron heating. With a decrease in amplitude of  $V_0$ , the magnitude of  $V_{DC}$  decreases, becoming more positive.

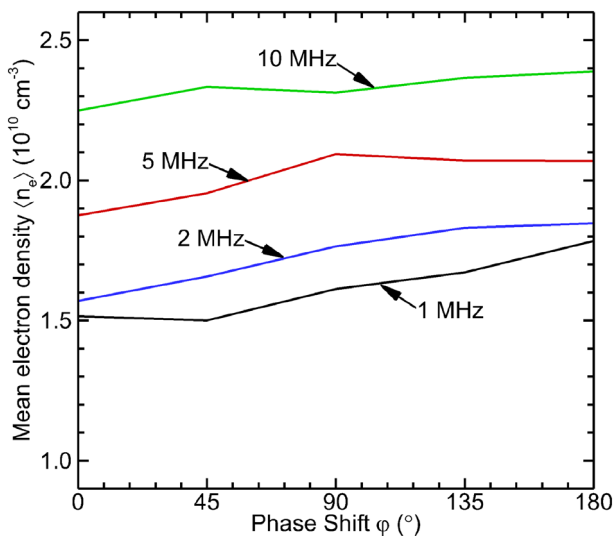


FIG. 12. Mean electron density as a function of phase shift  $\varphi$  for fundamental frequencies  $f_0 = 1\text{--}10\text{ MHz}$  at constant applied power.

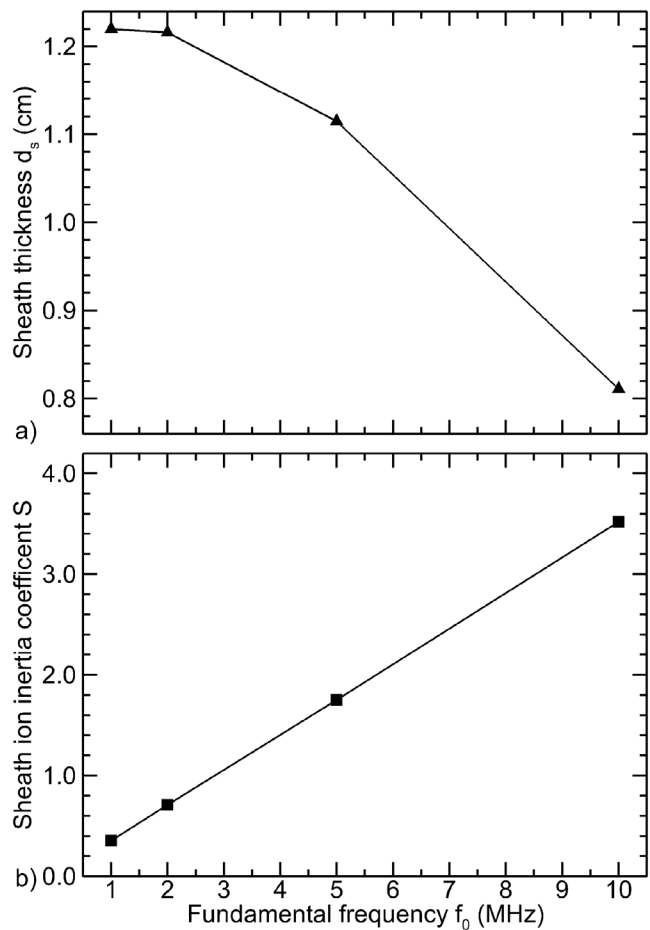


FIG. 13. Sheath properties as a function of fundamental frequency  $f_0$  for  $\varphi = 0^\circ$  at constant power. (a) Sheath thickness  $d_s$  and (b) sheath ion inertia coefficient  $S$ .

The average ion energies onto the wafer are shown in Fig. 14(b) as a function of phase shift  $\varphi$  for  $f_0 = 1\text{--}10\text{ MHz}$ . The corresponding IEADs as a function of phase shift  $\varphi$  for  $f_0 = 1$  and  $f_0 = 10\text{ MHz}$  are shown in Fig. 15. As when holding  $V_0$  constant, for higher frequencies the average ion energies scale with the magnitude of  $V_{DC}$  due to the inability of the ions to dynamically react to the transients in applied voltage. For  $f_0 = 10$  and  $f_0 = 5\text{ MHz}$ , this leads to a decrease in average energy onto the wafer with increasing phase angle. As with constant voltage, at low frequencies  $f_0$ , the average ion energies are poorly correlated (and, in fact, anti-correlated) with  $V_{DC}$  and instead reflect the maximum sheath potentials.

As a result of the applied voltage no longer being constant, the resulting average ion energies are strong functions of phase shift  $\varphi$  for fundamental frequencies  $f_0$ . For example, the mean energies at  $1\text{ MHz}$  are larger than those at  $10\text{ MHz}$  by a factor of 2 for  $\varphi = 0^\circ$  and  $4.5^\circ$  at  $\varphi = 180^\circ$ . These similarities and differences in mean ion energy between the constant voltage and constant power cases translate to the respective IEADs. At the lowest frequency ( $f_0 = 1\text{ MHz}$ ), the IEADs for  $\varphi = 0$  and  $180^\circ$  are more monoenergetic, reflecting the applied waveforms. The shapes of the applied voltage for these phase shifts

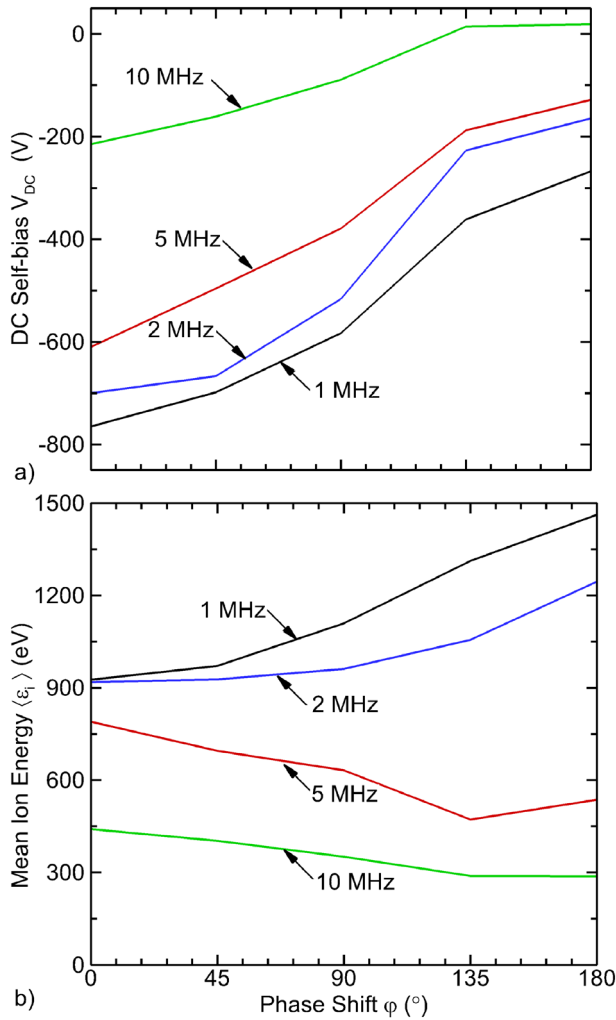


FIG. 14. Plasma parameters as a function of phase shift  $\phi$  for fundamental frequencies  $f_0 = 1$ –10 MHz at constant power. (a) DC self-bias and (b) mean ion energy delivered to the wafer.

roughly consist of a plateau and a singular well-defined short excursion to a maximum at  $\phi = 0^\circ$  and to a minimum at  $\phi = 180^\circ$ . The intermediate cases ( $\phi = 45^\circ, 90^\circ,$  and  $135^\circ$ ) do not have the similar monoenergetic structures as the applied waveforms themselves do not predominantly consist of a stable voltage plateau or singular peak.

Desired anisotropic etch profiles require a balance of polymer deposition and activation energy delivered by ions and hot neutrals whose rates are largely determined but the magnitude of the reactive fluxes arriving on the surface. The generation of oxide-polymer-complexes, which enables selective removal of the  $\text{SiO}_2$  is correlated with the incident flux of the polymerizing  $\text{C}_x\text{F}_y$  gas phase species, which are shown as a function of  $\phi$  and  $f_0$  in Fig. 16(a). The overall trends are that polymerizing fluxes are weak functions of phase angle  $\phi$  while generally increasing with increasing  $f_0$  on the bottom electrode. With increasing  $f_0$ , a larger proportion of bias power is dissipated by electron heating, which then produces a larger rate of

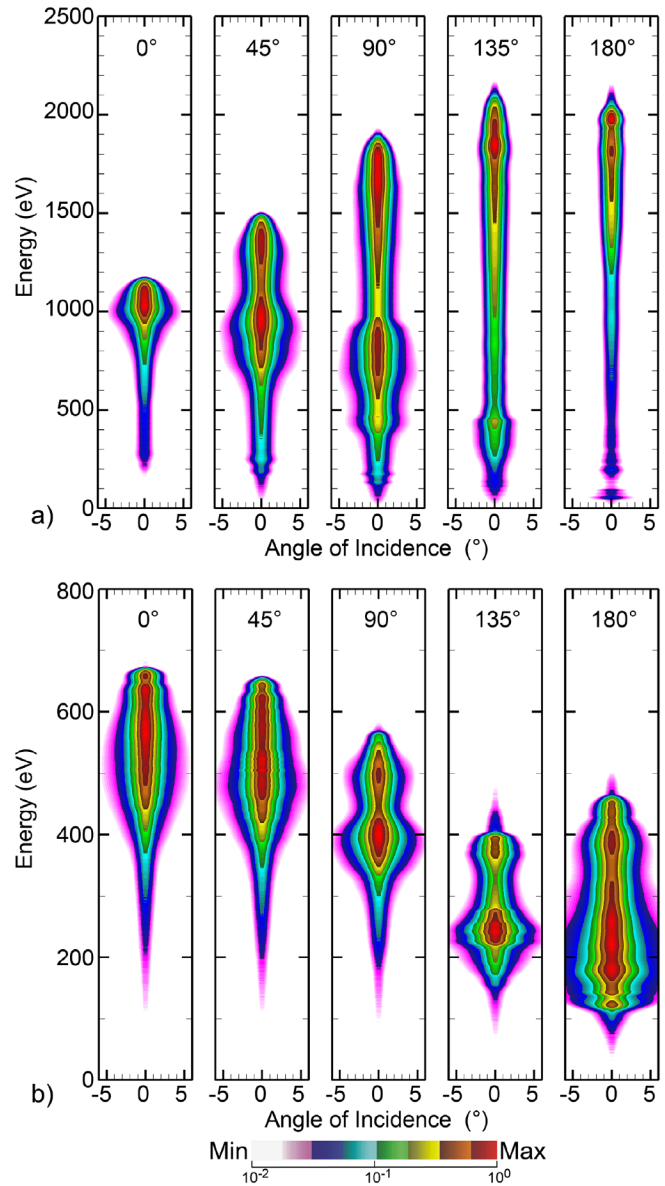
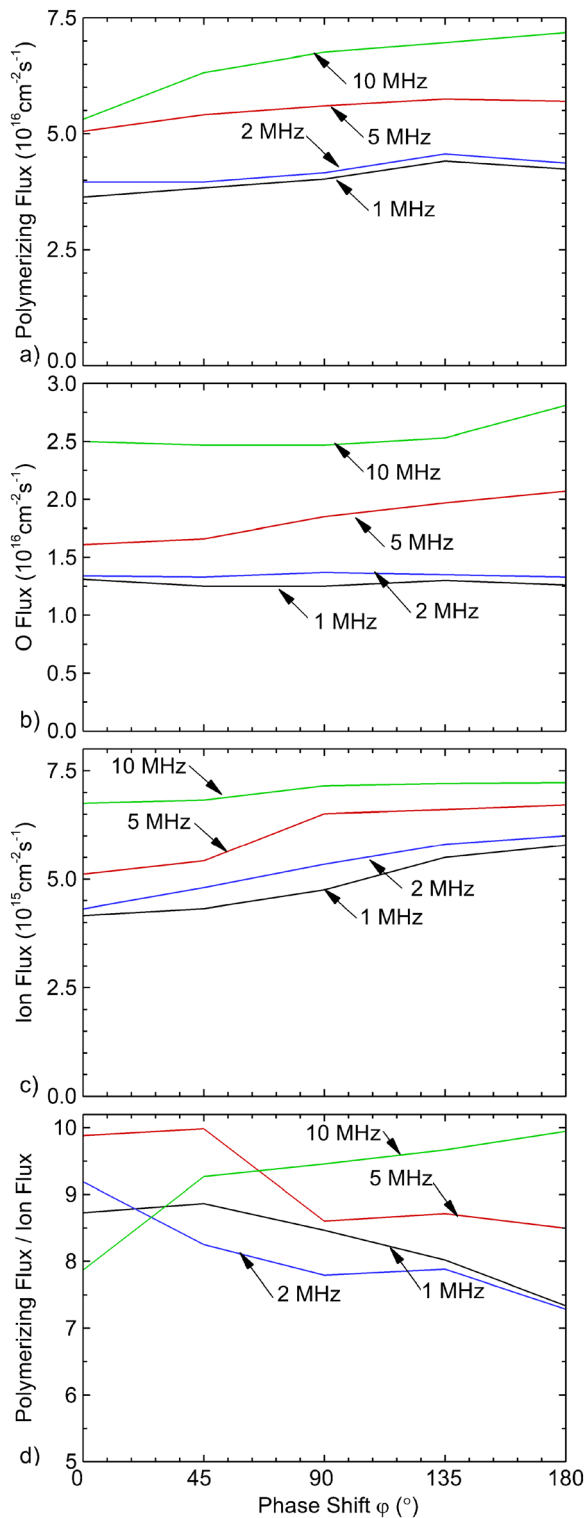


FIG. 15. IEADs as a function of phase shift  $\phi$  with constant power for fundamental frequencies (a)  $f_0 = 1$  and (b) 10 MHz. Values are plotted on a two-decade log scale.

dissociation of the  $\text{CF}_4$  feedstock gas. With increasing phase angle, the sheath is collapsed for a greater fraction of the cycle, thereby moving the effective (time average) sheath edge closer to the wafer. This shift in sheath edge places radical production closer to the wafer, and so increases fluxes.

The thickness of the polymer layer by deposition is balanced by chemical, isotropic etching by O radicals and anisotropic sputtering by directional ions. The time and spatial average of fluxes to the wafer of atomic oxygen, O, the most prevalent oxygen radical are shown in Fig. 16(b). The general trends reflect those of the polymerizing fluxes [Fig. 16(a)] that increase with  $\phi$  and  $f_0$ .



**FIG. 16.** Fluxes to the wafer as a function of phase shift  $\varphi$  for fundamental frequencies  $f_0 = 1$  to 10 MHz while keeping power constant: (a) total polymerizing flux, (b) O-atom flux, (c) total ion flux, and (d) ratio of polymerizing flux to ion flux.

The magnitude of the ion flux, shown in Fig. 16(c), has a first order effect on etch rates and feature quality. Applied electric fields directly influence charged particle transport, whereas electron impact dissociation, excitation, and ionization are at least one step removed as these phenomena occur as a result of electron collisions following their acceleration by electric fields. The dominant mechanism for ion power deposition is through sheath acceleration, which assuming a collisionless sheath, is proportional to the product of ion flux and incident ion energy. Assuming a constant fraction of power deposition by ion acceleration, a decrease in incident ion energy would necessitate an increase in ion flux to maintain the desired power. This is the trend for  $f_0 = 5$  and 10 MHz in which the trend of ion-flux with phase angle is opposite that of the ion energy. This explanation fails to capture the low frequency behavior in ion flux where an increasing fraction of the constant power deposition is due to electron heating.

**V. SiO<sub>2</sub> ETCHING AT CONSTANT POWER**

To characterize the consequences of reactant fluxes and IEADs on SiO<sub>2</sub> etch properties, profile simulations were performed for  $f_0 = 1$  and 10 MHz for phase angles  $\varphi = 0^\circ - 180^\circ$  while maintaining constant power. The resulting features for  $f_0 = 1$  MHz are shown in Fig. 17.

For constant processing time, etching through the entire 3000 nm thick SiO<sub>2</sub> layer only occurred for  $\varphi = 180^\circ$ , while for  $\varphi = 0^\circ$  the final etch depth is 1600 nm. The total relative etch rates are 0.53, 0.6, 0.78, 0.93, and 1.0 for  $\varphi = 0^\circ, 45^\circ, 90^\circ, 135^\circ,$  and  $180^\circ$ , respectively. This trend is directly correlated with the trend in incident ion energy. Higher ion energies generally more rapidly remove SiO<sub>2</sub> by direct or chemically enhanced sputtering and retain their ability to do so after losing energy to grazing sidewall collisions. The profiles produced by IEADs at higher  $\varphi$  have more desirable characteristics such as straighter sidewalls and less overall bowing. This benefit is a direct consequence of the narrower angular distribution of the incident ions. The SiO<sub>2</sub> etch mechanism contains a SiO<sub>2</sub>-polymer complex that requires fluorocarbon radical fluxes as reactants. Since these fluxes have a small increase with  $\varphi$  [Fig. 16(a)], the increased availability of reactants could also play a role in the increased etch rate if the etch progression is flux limited as is often the case in HAR features.

The results of the feature etching for  $f_0 = 10$  MHz are shown in Fig. 18. The overall etch rates are similar to those at  $f_0 = 1$  MHz while the incident ion energies are significantly lower overall. The trend in etch depth with phase angle is the opposite to that for  $f_0 = 1$  MHz. With  $f_0 = 10$  MHz, etch rates mildly decrease with increasing phase angle  $\varphi$  while increasing for  $f_0 = 1$  MHz. These trends most directly follow from both the average ion energies and maximum ion energies trending higher with increasing phase angle  $\varphi$  at  $f_0 = 1$  MHz while decreasing at  $f_0 = 10$  MHz. A secondary effect is that ion fluxes are nearly constant with increasing phase angle at  $f_0 = 10$  MHz while increasing at  $f_0 = 1$  MHz. With chemical and physical sputtering rates depending on ion energy as  $\epsilon^{1/2}$ , large increases in ion energy are required for significant increases in etch rates. That said, the likelihood for specular scattering from side walls increases with increasing ion energy, and so more energy is retained deeper into the feature upon grazing collisions with sidewalls. On the other hand, for otherwise constant, non-rate limiting conditions, etch rates increase linearly with increases in ion flux.

While certainly an important parameter, ion energy is not the sole determining factor for etch rate. The etch process is based on a sensitive balance of surface passivation, activation, and removal by

01 April 2024 12:15:40

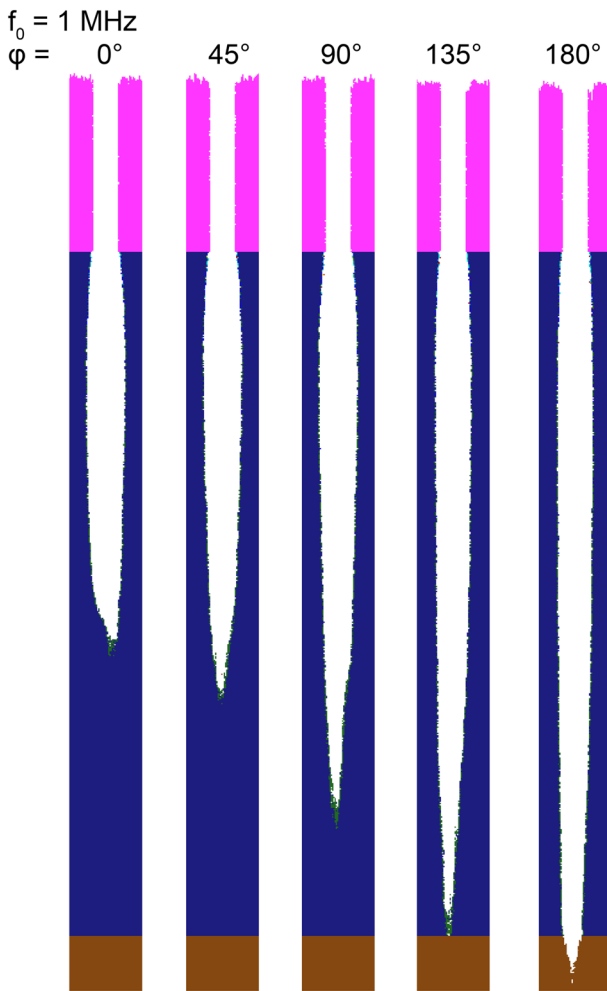


FIG. 17. Predictions for etch profiles in  $\text{SiO}_2$  at constant power with fundamental frequency  $f_0 = 1$  MHz and varying phase angles  $\varphi$ .

fluxes of neutrals, ions, and hot neutrals (generated by ions neutralizing during surface collisions). For each fundamental frequency, the ratio of these fluxes as function of  $\varphi$  is relatively constant, as shown in Fig. 16(d). Although ion energy and fluxes determine overall rate of etching, the shape of the feature (e.g., sidewall slope, bowing) depends on relative rates of passivation by deposition, etching, and sputtering. For example, for  $f_0 = 10$  MHz, despite the higher etch rate with increasing phase angle, the features generally have less bowing, an effect that may be attributable to a larger ratio of polymerizing flux to ion flux. Large fluxes of passivating species typically produce more tapered features.

## VI. CONCLUDING REMARKS

Coupled reactor and feature scale simulations were performed to investigate the consequences of the fundamental driving frequency  $f_0$  on the relation between DC self-bias  $V_{\text{DC}}$ , incident ion energy onto the wafer, and reactive fluxes in dielectric etch processes using tailored voltage waveforms as a power source. For a set of waveforms based on

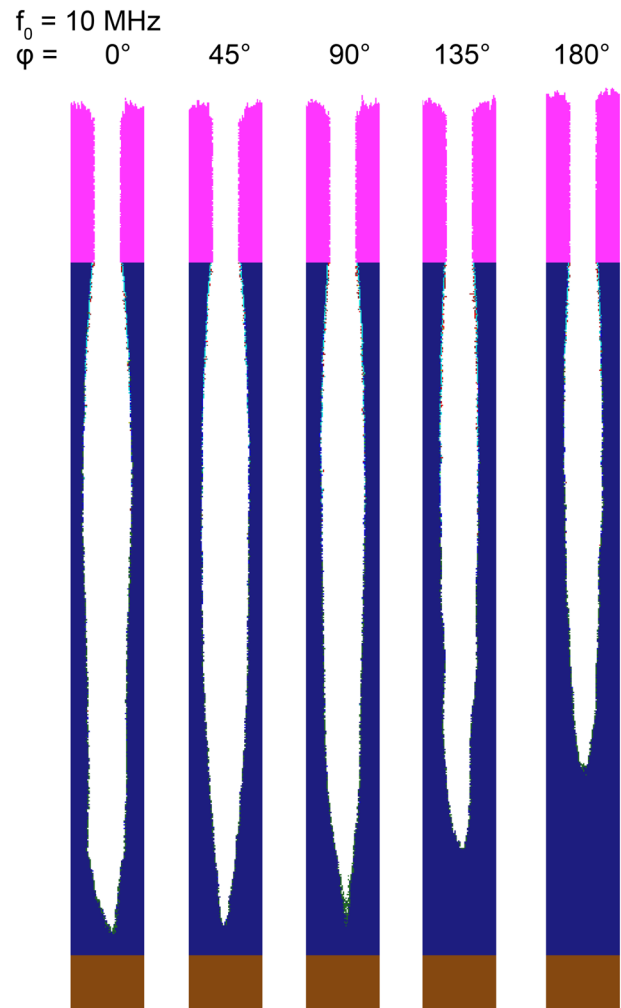


FIG. 18. Predictions for etch profiles in  $\text{SiO}_2$  at constant power with fundamental frequency  $f_0 = 10$  MHz and varying phase angles  $\varphi$ .

consecutive harmonics for which the relative phase angle  $\varphi$  was varied from  $0^\circ$  to  $180^\circ$ , gas phase simulations were performed using fundamental frequencies  $f_0 = 1, 2, 5,$  and  $10$  MHz. While plasma conditions were found to differ when holding either voltage or power constant, the trends in  $V_{\text{DC}}$  were qualitatively similar for the two scenarios. The magnitude of  $V_{\text{DC}}$  decreases (a negative bias becoming more positive) with increasing  $\varphi$  for all  $f_0$  at constant voltage as well as power. Due to ion inertia, in the high frequency regime ion fluxes to the substrate are dominated by time average quantities such as  $V_{\text{DC}}$ . At low  $f_0$ , the ions are able to react to transient characteristics in the sheath such as local extremes in the sheath potential directly produced by the applied tailored voltage waveforms.

The consequences of inertial effects on IEADs as a function of sinusoidal bias frequency are well known. The thick sheath regime corresponding to high frequency and large ion mass produces a single peaked IEAD. The thick sheath regime corresponding to low frequency and small mass produces a double peaked (bimodal) IEAD.

The extension of these dependencies to VWT power sources is not straightforward due to the intrinsically more complex sheath structure and harmonic content of the applied voltages. The majority of sheath theories are based on applying a single sinusoidal voltage. VWT applies several discrete frequencies that induce additional nonlinearities. The extension to square-wave pulsing with even more Fourier derived frequencies present additional theoretical challenges.

The results of this study suggest that scaling of  $V_{DC}$  produced by processes akin to the electrical asymmetry, a common goal sought when using voltage waveform tailoring, is particularly sensitive to the frequency regime of  $f_0$ . Low values of  $f_0$  can result in significantly different trends of incident ion energy as a function of phase angle compared to high values of  $f_0$ . Incident ion energy is closely correlated with the  $V_{DC}$  self-bias at high values of  $f_0$ , maximum at  $\varphi = 0^\circ$  and minimum at  $\varphi = 180^\circ$ . For low values of  $f_0$ , this correlation dissipates, and incident ion energy is instead dominated by the sheath dynamics of the applied voltage waveforms, maximum at  $\varphi = 180^\circ$  and minimum at  $\varphi = 0^\circ$ .

The trends in ion energy (and IEADs) as a function of  $f_0$  and  $\varphi$  directly impact the HAR etch process. Although the observations and conclusions made in this work are highly dependent on power deposition, plasma density, chemical composition, and geometry, these observations also open additional avenues for process control. With three-dimensional structures and atomic layer resolution already dominating industrial plasma etching processes, additional control strategies are required to achieve the desired critical dimensions. With frequency agile power supplies becoming more available, the combination of using VWT while varying fundamental frequency and phase angle provide new control opportunities.

The authors are not aware of the availability of experimental data for a 1-to-1 comparison to the results discussed here. The modeling platform that has been used in this investigation is accurate in the sense that results using the model have been validated against experiments performed in many types of reactors and chemistries. The degree of accuracy for any specific investigation is difficult to assess when that investigation is in a parameter space that has not yet been, or not been fully, experimentally investigated. Modeling is extremely valuable in attempting to reproduce experimental results to confirm theories, tasks that are typically performed in simpler geometries and less complex gas mixtures. This practice reduces the uncertainties associated with incomplete reaction mechanisms and produced by geometrical effects, and so enables one to focus on the theory. Modeling was used here to investigate a parameter space that has not been fully experimentally characterized for conditions that are close to those used in applications to help guide those applications. In doing so, the expected precision of the computational investigation is likely less than more focused investigations. The value of investigations of this type is in developing scaling laws that are generally applicable to guide technology development.

## ACKNOWLEDGMENTS

This work was supported by Samsung Electronics Ltd and Tokyo Electronics America. These results were also based upon work supported by the U.S. Department of Energy, Office of Science, Office of Fusion Energy Sciences under Award No. DE-SC0020232 and supported by the National Science Foundation (No. PHY-2009219).

## AUTHOR DECLARATIONS

### Conflict of Interest

The authors have no conflicts to disclose.

### Author Contributions

**Florian Krüger:** Conceptualization (lead); Formal analysis (lead); Investigation (lead); Methodology (lead); Writing – original draft (lead). **Hyunjae Lee:** Resources (equal); Supervision (equal); Writing – review & editing (equal). **Sang Ki Nam:** Resources (equal); Supervision (equal); Writing – review & editing (equal). **Mark J. Kushner:** Funding acquisition (equal); Project administration (equal); Supervision (equal); Writing – review & editing (equal).

## DATA AVAILABILITY

The data that support the findings of this study are contained in the paper and are available from the corresponding author upon reasonable request.

## REFERENCES

- <sup>1</sup>V. M. Donnelly and A. Kornblit, *J. Vac. Sci. Technol.*, **A 31**, 050825 (2013).
- <sup>2</sup>Y. Li, *IEEE Solid-State Circuits Mag.* **12**, 56 (2020).
- <sup>3</sup>S.-J. Chung, P. Luan, M. Park, A. Metz, and G. S. Oehrlein, *J. Vac. Sci. Technol.*, **B 41**, 062201 (2023).
- <sup>4</sup>S. Rauf and A. Balakrishna, *J. Vac. Sci. Technol.*, **A 35**, 021308 (2017).
- <sup>5</sup>B. Wu, A. Kumar, and S. Pamarthy, *J. Appl. Phys.* **108**, 051101 (2010).
- <sup>6</sup>G. A. Skarphedinsson and J. T. Gudmundsson, *Plasma Sources Sci. Technol.* **29**, 084004 (2020).
- <sup>7</sup>S. Brandt, B. Berger, E. Schüngel, I. Korolov, A. Derzsi, B. Bruneau, E. Johnson, T. Lafleur, D. O'Connell, M. Koepke, T. Gans, J.-P. Booth, Z. Donkó, and J. Schulze, *Plasma Sources Sci. Technol.* **25**, 045015 (2016).
- <sup>8</sup>P. Hartmann, L. Wang, K. Nösger, B. Berger, S. Wilczek, R. P. Brinkmann, T. Mussenbrock, Z. Juhasz, Z. Donkó, and A. Derzsi, *J. Phys. D* **54**, 255202 (2021).
- <sup>9</sup>Z. Donkó, A. Derzsi, M. Vass, J. Schulze, E. Schuengel, and S. Hamaguchi, *Plasma Sources Sci. Technol.* **27**, 104008 (2018).
- <sup>10</sup>T. Lafleur, *Plasma Sources Sci. Technol.* **25**, 013001 (2015).
- <sup>11</sup>J. Wang, S. Dine, J.-P. Booth, and E. V. Johnson, *J. Vac. Sci. Technol. A* **37**, 021303 (2019).
- <sup>12</sup>F. Schmidt, J. Schulze, E. Johnson, J.-P. Booth, D. Keil, D. M. French, J. Trieschmann, and T. Mussenbrock, *Plasma Sources Sci. Technol.* **27**, 095012 (2018).
- <sup>13</sup>J. Schulze, E. Schüngel, Z. Donkó, and U. Czarnetzki, *Plasma Sources Sci. Technol.* **20**, 015017 (2011).
- <sup>14</sup>P. Saikia, H. Bhuyan, M. Escalona, M. Favre, B. Bora, M. Kakati, E. Wyndham, R. S. Rawat, and J. Schulze, *J. Appl. Phys.* **123**, 183303 (2018).
- <sup>15</sup>C. Qu, Y. Sakiyama, P. Agarwal, and M. J. Kushner, *J. Vac. Sci. Technol.*, **A 39**, 052403 (2021).
- <sup>16</sup>S. J. Lanham, J. Polito, Z. Xiong, U. R. Kortshagen, and M. J. Kushner, *J. Appl. Phys.* **132**, 073301 (2022).
- <sup>17</sup>S. Huang, S. Shim, S. K. Nam, and M. J. Kushner, *J. Vac. Sci. Technol.*, **A 38**, 023001 (2020).
- <sup>18</sup>M. J. Kushner, *J. Phys. D* **42**, 194013 (2009).
- <sup>19</sup>H. K. Kim, T. S. Kim, J. Lee, and S. K. Jo, *Phys. Rev. B* **76**, 165434 (2007).
- <sup>20</sup>A. V. Phelps and Z. L. Petrovic, *Plasma Source Sci. Technol.* **8**, R21 (1999).
- <sup>21</sup>S. Huang, C. Huard, S. Shim, S. K. Nam, I.-C. Song, S. Lu, and M. J. Kushner, *J. Vac. Sci. Technol.*, **A 37**, 031304 (2019).
- <sup>22</sup>C. M. Huard, S. Sriraman, A. Paterson, and M. J. Kushner, *J. Vac. Sci. Technol.*, **A 36**, 06B101 (2018).
- <sup>23</sup>J. Schulze, Z. Donkó, B. G. Heil, D. Luggenhölscher, T. Mussenbrock, R. P. Brinkmann, and U. Czarnetzki, *J. Phys. D* **41**, 105214 (2008).

- <sup>24</sup>U. Czarnetzki, J. Schulze, E. Schüngel, and Z. Donkó, *Plasma Sources Sci. Technol.* **20**, 024010 (2011).
- <sup>25</sup>S. J. Doyle, A. R. Gibson, R. W. Boswell, C. Charles, and J. P. Dedrick, *Plasma Sources Sci. Technol.* **29**, 124002 (2020).
- <sup>26</sup>B. G. Heil, U. Czarnetzki, R. P. Brinkmann, and T. Mussenbrock, *J. Phys. D* **41**, 165202 (2008).
- <sup>27</sup>L. P. Beving, M. M. Hopkins, and S. D. Baalrud, *Plasma Sources Sci. Technol.* **31**, 084009 (2022).
- <sup>28</sup>B. G. Heil, R. P. Brinkmann, and U. Czarnetzki, *J. Phys. D* **41**, 225208 (2008).
- <sup>29</sup>T. Shirafuji and K. Denpoh, *Jpn. J. Appl. Phys., Part 1* **57**, 06JG02 (2018).
- <sup>30</sup>B. Mancinelli, L. Prevosto, J. C. Chamorro, F. O. Minotti, and H. Kelly, *Plasma Chem. Plasma Process.* **38**, 147 (2018).
- <sup>31</sup>O. Murillo, A. S. Mustafae, and V. S. Sukhomlinov, *Tech. Phys.* **64**, 1308 (2019).
- <sup>32</sup>M. S. Benilov and N. A. Almeida, *Phys. Plasmas* **26**, 123505 (2019).
- <sup>33</sup>S. D. Baalrud, B. Scheiner, B. T. Yee, M. M. Hopkins, and E. Barnat, *Plasma Sources Sci. Technol.* **29**, 053001 (2020).
- <sup>34</sup>R. P. Brinkmann, *J. Phys. D* **42**, 194009 (2009).
- <sup>35</sup>R. P. Brinkmann, *J. Phys. D* **44**, 042002 (2011).
- <sup>36</sup>M. Klich, J. Löwer, S. Wilczek, T. Mussenbrock, and R. P. Brinkmann, *Plasma Sources Sci. Technol.* **31**, 045014 (2022).